Correspondence and
requests for materials
should be addressed to
SLC. (shulei@uow.edu.
au)

A facile approach to synthesize stable CNTs@MnO electrocatalyst for high energy lithium oxygen batteries

Wen-Bin Luo[1], Shu-Lei Chou[1], Jia-Zhao Wang[1], Yu-Chun Zhai[2] & Hua-Kun Liu[1]

[1]Institute for Superconducting and Electronic Materials, University of Wollongong, Wollongong, NSW 2522, Australia, [2]School of Materials and Metallurgy, Northeastern University, Shenyang 110004, China.

A composite of manganese monoxide loaded onto carbon nanotubes (CNTs@MnO) has been synthesized by a facile approach, in which the CNTs form a continuous conductive network connecting the electrocatalyst MnO nanoparticles together to facilitate good electrochemical performance. The electrocatalyst MnO shows favourable rechargeability, and good phase and morphology stability in lithium oxygen batteries. Excellent cycling performance is also demonstrated, in which the terminal voltage is higher than 2.4 V after 100 cycles at 0.4 mA cm^{-2}, with 1000 mAh g^{-1}(composite) capacity. Therefore, this hybrid material is promising for use as a cathode material for lithium oxygen batteries.

T he demand for sustainable and clean energy is becoming more and more critical, owing to the emergence of applications such as electric vehicles and the many new types of portable electronic devices currently available. Therefore, the search for the next generation of energy-storage materials and devices is extremely important. The lithium air battery is one of the most promising ones because of its potential for very high-energy density, exceeding that of any other existing energy storage system, owing to its inexhaustible and ubiquitous source of oxygen. The electrocatalysts for the oxygen reduction reaction (ORR, $O_2 + 2Li^+ + 2e^- \rightarrow Li_2O_2$) and the oxygen evolution reaction (OER, $Li_2O_2 \rightarrow O_2 + 2Li^+ + 2e^-$) play a key role in improving the power density, cycling stability, and energy efficiency, and are key enablers for practical rechargeable lithium oxygen batteries. Therefore, it is necessary to develop stable and efficient electrocatalysts with proper morphology for the oxygen reduction and oxygen evolution reactions in the lithium air battery[1–7]. The electrocatalysts can be roughly classified into the following three categories: (1) porous carbon materials, including carbon black, nanostructured carbon, functionalized carbon, and graphene, which, strictly speaking, are not electrocatalysts, but act as electro-catalyst support or as an electrically conductive additive[8–14]; (2) precious metals (alloys), for example, Pt, Au, Ag, and Pd, which might make a lithium air battery economically impractical[15–19]; and (3) transition metal oxides, mainly manganese-based oxides and composites, and cobalt oxides[9,20–24], which have attracted great attention because of their potential low cost and rich resources. Among these catalysts, various structures and morphologies of manganese oxide, such as MnO_2 nanowires, MnO_2 hollow spheres, and MnO_2 nanorods, have been synthesized and used as cathode catalysts for lithium air batteries[20]. It is worth pointing out, however, that MnO_2, although a very promising cathode material for the lithium primary battery, cannot be stably cycled between 1.5 – 4.0 V vs. Li^+/Li in the lithium ion rechargeable battery system. MnO_2 takes part in the reaction to form intermediate products with unexpected morphology, which will influence the electrocatalyst performance[25]. Therefore, MnO_2 would not be a good choice as a stable electrocatalyst for the lithium air battery.

On the other hand, many reports have also revealed that the supporting materials for the electrocatalyst are also one of the key factors controlling the performance of the oxygen electrode[2,6,18,26–28]. The application of carbon nanotubes (CNTs) in electrical materials has attracted intense research interest because of their extraordinary thermal and mechanical stability, as well as the high electronic conductivity of CNTs. Homogeneously dispersing CNTs on the surface of the active materials has the following advantages: (1) the CNTs form a continuous conductive network on the bulk of the electrode to improve the cycling performance; (2) the CNTs improve the adsorption and penetration of the electrolyte on the surface of the electroactive materials to facilitate the electrode reaction kinetics; and (3) the CNTs can act as a buffer among the electroactive materials due to their superior resiliency, restraining cracking and crumbling, and maintaining the integrity of the electrode[29].

Therefore, in this work, we investigated stable manganese monoxide (MnO) decorated on carbon nanotube catalyst support as oxygen electrocatalyst in lithium oxygen batteries, and conducted further research on the
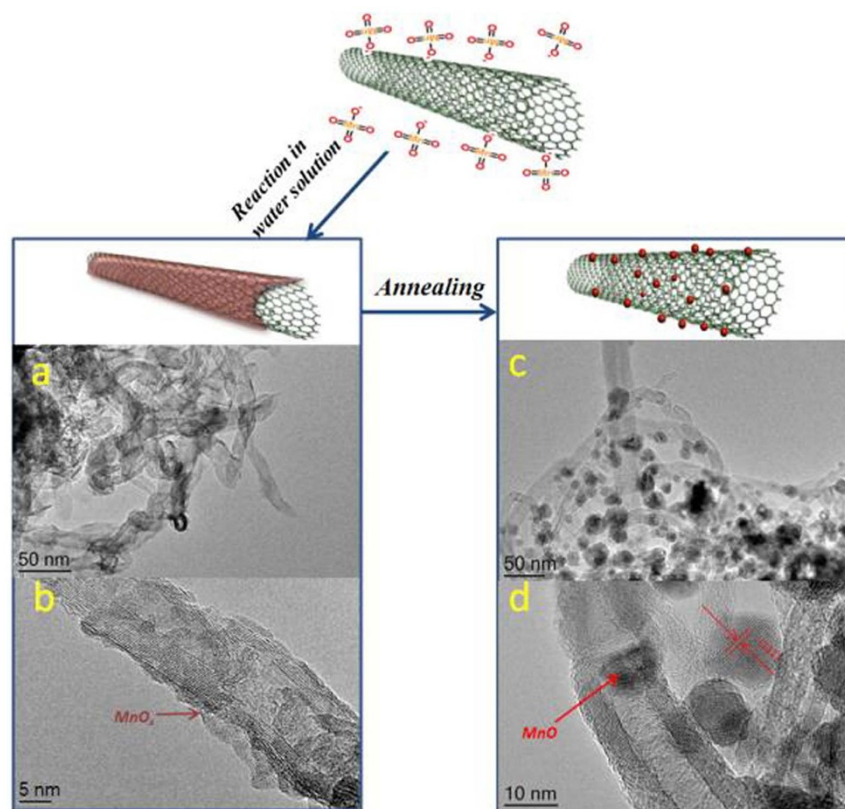
Figure 1 | Schematic flow-process diagram of the whole process, with corresponding HRTEM images of the CNTs@MnO$_x$ (a, b), and CNTs@MnO (c, b) composites.

deposition of reaction products and decomposition mechanism in the electrocatalysis process using the hydrodynamic rotating ring-disk electrode (RRDE) technique in non-aqueous solution. Multiwall carbon nanotubes with high electronic conductivity were used as the supporting materials for the electrocatalyst, and nanosized MnO was successfully deposited on them to catalyse the chemical reactions with high capacity. The composite material with its network structure shows favourable rechargeability and good stability in the air electrode for lithium oxygen batteries.

Results

Structure and Morphology Analysis. The general process for the fabrication of CNTs@MnO composite is illustrated in Fig. 1. Typically, MnO$_4{}^{-1}$ anions react with multiwall CNTs in water solution to produce an amorphous Mn-based precursor MnO$_x$ layer that forms a coating on the CNTs, as can be confirmed by the high resolution transmission electron microscope (HRTEM) images in Fig. 1(a, b). Then, the CNTs@MnO composite is obtained by annealing the intermediate product at 500°C for 6 h in a reducing H$_2$/Ar atmosphere. MnO nanoparticles with sizes in the range of 20 nm are uniformly anchored on and connected with the CNTs to form a continuous conductive network, which can also be confirmed by Fig. 1(c, d).

Information on the process was obtained from the associated X-ray diffraction (XRD) and X-ray photoelectron spectroscopy (XPS) measurements (Fig. 2). In Fig. 2(a), apart from the peaks of the CNTs at 26°, three weak peaks (marked with asterisks) at 2θ around 12°, 37°, and 66° are observed in the intermediate product CNTs@MnO$_x$, which mainly can be indexed to α-MnO$_2$, including its amorphous phase. After annealing at 500°C in Ar/H$_2$ atmosphere, pure cubic MnO was then obtained, which is indexed to a pure cubic phase (PDF:07 – 0230), and no impurity peaks can be found. The MnO cubic phase can also be confirmed from the lattice fringes corres-

ponding to the (111) planes in the HRTEM image shown in Fig. 1(d). In Fig. 2(b), the Mn 2p peak of the original CNTs@MnO$_x$ can be deconvoluted into two different components. The most intense peak, at 642.5 eV, is assigned to Mn 2p$_{3/2}$, which, together with the component at 653.9 eV that corresponds to Mn 2p$_{1/2}$, is a signature of Mn (IV) on the surface of the CNTs@MnO$_x$ composite. After reduction in Ar/H$_2$ atmosphere, the peaks of Mn 2p$_{3/2}$ and Mn 2p$_{1/2}$ left shift to 642.2 eV and 653.4 eV, respectively, as is characteristic of MnO, revealing that the Mn (IV) has been reduced to Mn (II). The samples were also investigated using Raman spectroscopy (Fig. S2 in the Supplementary Information). After coating with the MnO$_x$ layer and reducing it to MnO particles on the outer surface of the CNTs, the characteristic Mn – O vibration modes of manganese oxides are located in the range of 580 – 670 cm^{-1}. The total weight of CNTs in the CNTs@MnO composite can be roughly calculated as 50% from the loss percentage in the thermogravimetric analysis (TGA) curves (Fig. S3).

Electrochemical characterization. The electrochemical properties of the CNTs@MnO were then examined in a lithium oxygen cell without conductive carbon black (Fig. S1 in the Supplementary Information), and all of the results for the specific capacities are calculated from the total composite mass in the cathode. The pure CNTs and CNTs@MnO$_x$ are included for comparison in Fig. 3(a), which shows the first discharge/charge voltage profiles of the electrodes with pure CNTs, and the CNTs@MnO$_x$ and CNTs@MnO composites at a current density of 0.1 mA cm^{-2}. Compared with the pure CNTs and the CNTs@MnO$_x$, we can clearly see that the CNTs@MnO composite shows excellent discharge/charge performance. The CNTs@MnO composite exhibits the improvement of the discharge capacity and the round-trip performance (the ratio of discharge to charge voltage) that is vital for electrochemical energy storage devices, delivering a discharge capacity of 6360 and
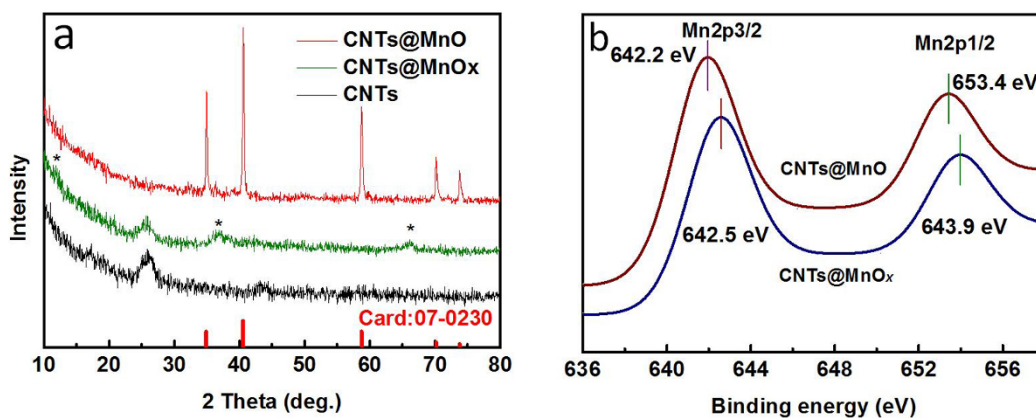
Figure 2 | (a) XRD results for CNTs, and the CNTs@MnO$_x$ and CNTs@MnO composites; (b) XPS results for the CNTs@MnO$_x$ and CNTs@MnO composites.

a charge capacity of 5510 mAh g^{-1}$_{(composite)}$ at 0.1 mA cm^{-2} current density. Furthermore, the discharge plateau of the CNTs@MnO composite is at 2.67 V, higher than those of the pure CNTs and CNTs@MnO$_x$, 2.53 and 2.55 V (specific capacity 2000 mAh g^{-1}$_{(composite)}$ positions), respectively. The charge voltage of the CNTs@MnO composite is also much lower than those of the CNTs and CNTs@MnO$_x$, showing the best round-trip performance. In Fig. 3(b), when the current density is increased to 0.2, 0.4, and 0.6 mA cm^{-2}, the CNTs@MnO composite also exhibits excellent discharge/charge performance, with 5916/4974, 4137/3905, and 2527/2293 mAh g^{-1}$_{(composite)}$, respectively. According to the capacity-limited cycling method that has recently come into widespread use[27], Fig. 3(c, d) respectively presents the discharge/charge and cycling performances of the CNTs@MnO composite at 0.4 mA cm^{-2} current density with a fixed specific capacity of 1000 mAh g^{-1}$_{(composite)}$. The ORR and OER profiles for the CNTs@MnO composite are shown over the whole process of discharge and charge. It exhibits a higher ORR potential and lower OER potential compared to the other samples, even after 100 cycles, and the voltage obtained at the discharge terminal is higher than 2.4 V for 100 cycles. Generally speaking, the CNTs@MnO composite exhibits excellent electrochemical performance in terms of both deposition and decomposition of discharge products, which might be attributed to substantial reaction sites for the reaction and deposition of nanocrystal products located between the MnO and the CNTs, resulting from surface defects together with the continuous three-dimensional (3D) electronically conductive network formed by the CNTs, as well as the efficient synergistic effects of the high catalyst reaction rates towards the ORR and OER processes from the MnO electrocatalyst.

Reaction mechanism. The rotating disk electrode (RDE) technique was used to investigate the ORR activities of three samples in O$_2$-saturated 0.1 M KOH electrolyte at a scan rate of 5 mV s^{-1}, including commercial Pt/C (10 wt% Pt on Vulcan XC-72), pure CNTs, and CNTs@MnO$_x$ and CNTs@MnO composites. As shown in the RDE curves in Fig. 4, the pure CNTs exhibited the lowest ORR electrocatalytic activity, while CNTs@MnO showed an enhanced ORR performance with positive onset potential and large current density compared to those of the CNTs@MnO$_x$ composite and commercial Pt/C. Furthermore, the RDE curves of Pt/C, pure CNTs, and the CNTs@MnO$_x$ and CNTs@MnO composites at various rotation speeds were collected to determine their ORR kinetic performances (details in Supplementary information)[30–32]. The corresponding Koutecky-Levich (K–L) plots (J^{-1} vs. $\omega^{-1/2}$) at various electrode potentials exhibited good linearity (inset images in Fig. 4). The linearity and parallelism of the K–L plots suggested first-order reaction kinetics with respect to the concentration of dissolved oxygen and similar electron transfer numbers for the ORR at different potentials[33–35]. The electron transfer number (n) of CNTs@MnO composite was calculated to be 3.8–4.0 from the slope of the K–L plot, indicating that CNTs@MnO favoured a 4e$^-$ oxygen reduction process, in contrast to the lower values of n for CNTs@MnO$_x$ (3.2–3.4) and pure CNTs (1.3–1.5). We can reach the conclusion that the CNTs@MnO composite shows much higher ORR catalytic activity than pure CNTs, CNTs@MnO$_x$, and commercial Pt/C, so that it might be a promising non-precious-metal-based catalyst.

To demonstrate the results of accurate and similar research on the ORR and OER processes in non-aqueous electrolyte, Figure 5(a) shows steady-state cyclic voltammograms (CVs) of the three sample electrodes in 1 M LiPF$_6$ in tetraethylene glycol dimethyl ether (TEGDME) under both argon saturated and oxygen saturated conditions with a scan rate of 20 mV s^{-1}. Obviously, no significant anodic or cathodic peak was observed for the CNTs@MnO composite with argon saturated electrolyte, which suggests that there are no corresponding chemical reactions proceeding in the whole process[36,37]. In the anodic scan process when the electrolyte was saturated with oxygen, however, the three electrodes show a current corresponding to the oxygen reduction process, in which CNTs@MnO showed enhanced reduction performance with positive onset potential and a large current density compared to those of the pure CNTs and CNTs@MnO$_x$ composite. In the following cathodic scan process, there is a substantial evolution current, while no evidence of such a current appears for either the pure CNTs or the CNTs@MnO$_x$ composite, which indicates that MnO plays a key role in the process of the oxygen evolution reaction.

To investigate the formation of the reaction products, linear sweep voltammograms (LSPs) were collected between 1.6 – 3.0 V with a scan rate of 5 mV s^{-1} at 900 rpm in O$_2$-saturated electrolyte, with the ring held at 3.5 V, as shown in Figure 5(b). In this technique, the intermediate or final products, O$^-$ or O$_2^-$, generated at the disk electrode could be accurately determined. It is found that CNTs@MnO also shows an enhanced reduction trend with positive onset potential and large current density compared to those of the pure CNTs and CNTs@MnO$_x$ composite, together with a high ring current corresponding to a high percentage of intermediate or final products.

To further understand the whole process of the CNTs@MnO hybrid reaction mechanism, ex-situ XRD was used to determine the phases of the reaction products in the cathode electrode at different discharge/charge states, as shown in Figure 6. The original XRD pattern for the as-prepared cathode electrode, consisting of CNTs@MnO coated onto glass fibre separator (GFS), exhibits several

obvious peaks corresponding to MnO phase. Compared with the original electrode, there is clear evidence of the presence of crystalline Li_2O_2 at the end of the first full discharge, which indicates that a large amount of discharge product has been deposited on the cathode electrode. At the end of charging, the Li_2O_2 cannot be detected, which is consistent with the results obtained by other groups, indicating the high reversibility of Li_2O_2 during cycling[6,15,17,38,39]. Meanwhile, the XRD patterns show that there is no big change in the MnO peaks after charge and discharge, indicating the stability of MnO as electrocatalyst, which is consistent with the results in Fig. S4. MnO and MnO_x were reacted with lithium ions to different degrees to test the catalyst stability in the working voltage window. In Fig. S4, MnO only exhibits less that 10 mAh g^{-1} specific capacity, much less than that of MnO_x (> 170 mAh g^{-1}), within the voltage window between 2.0–3.5 V. Therefore, the conclusion we reach from the XRD results is that the main reaction product Li_2O_2 can be decomposed and that MnO electrocatalyst maintains highly stable catalyst function over the whole discharge/charge process.

The morphologies of the cathodes and a schematic diagram showing the different discharge/charge states are shown in Fig. 7. In the discharge process, the reaction produces Li_2O_2 nanocrystals deposited on the cathode electrode, which can be confirmed by the corresponding scanning electron microscope (SEM) images in (i, ii). In the charge process, Li_2O_2 deposits are decomposed because of the role of the MnO electrocatalyst, which indicates the lower charge potential platform, resulting in the disappearance of the obvious aggregates in the corresponding image (iii and iv), which is in agreement with the XRD results. The schematic diagram summarizes the whole process of discharge and charge. It is worth to point out that the reactions are happening in the interfaces of solid (electrode materials), liquid (electrolyte), and gas (oxygen) phases. Therefore, any tiny factors may influence the performance of the whole ORR and OER processes in the cell. Nevertheless, MnO electrocatalyst coating on CNTs builds an efficient composite. It promotes high energy density in the lithium oxygen batteries because of the abundant deposition and positions of reaction products.

Conclusions. CNTs@MnO electrocatalyst was obtained by annealing the intermediate product CNTs@MnO_x at 500°C for 6 h in a reducing H_2/Ar atmosphere. The annealed product shows favourable rechargeability and good stability, along with an electronically conductive network, in lithium oxygen cells. MnO nanoparticles coated on the walls of the CNTs play a key electrocatalyst role in the ORR and OER reactions and influence the reaction product deposition and decomposition, as evidenced by the results of the hydrodynamic investigation techniques. CNTs@MnO composite shows excellent discharge/charge performance in lithium oxygen cells, delivering 6360/5510, 5916/4974, 4137/3905, and 2527/
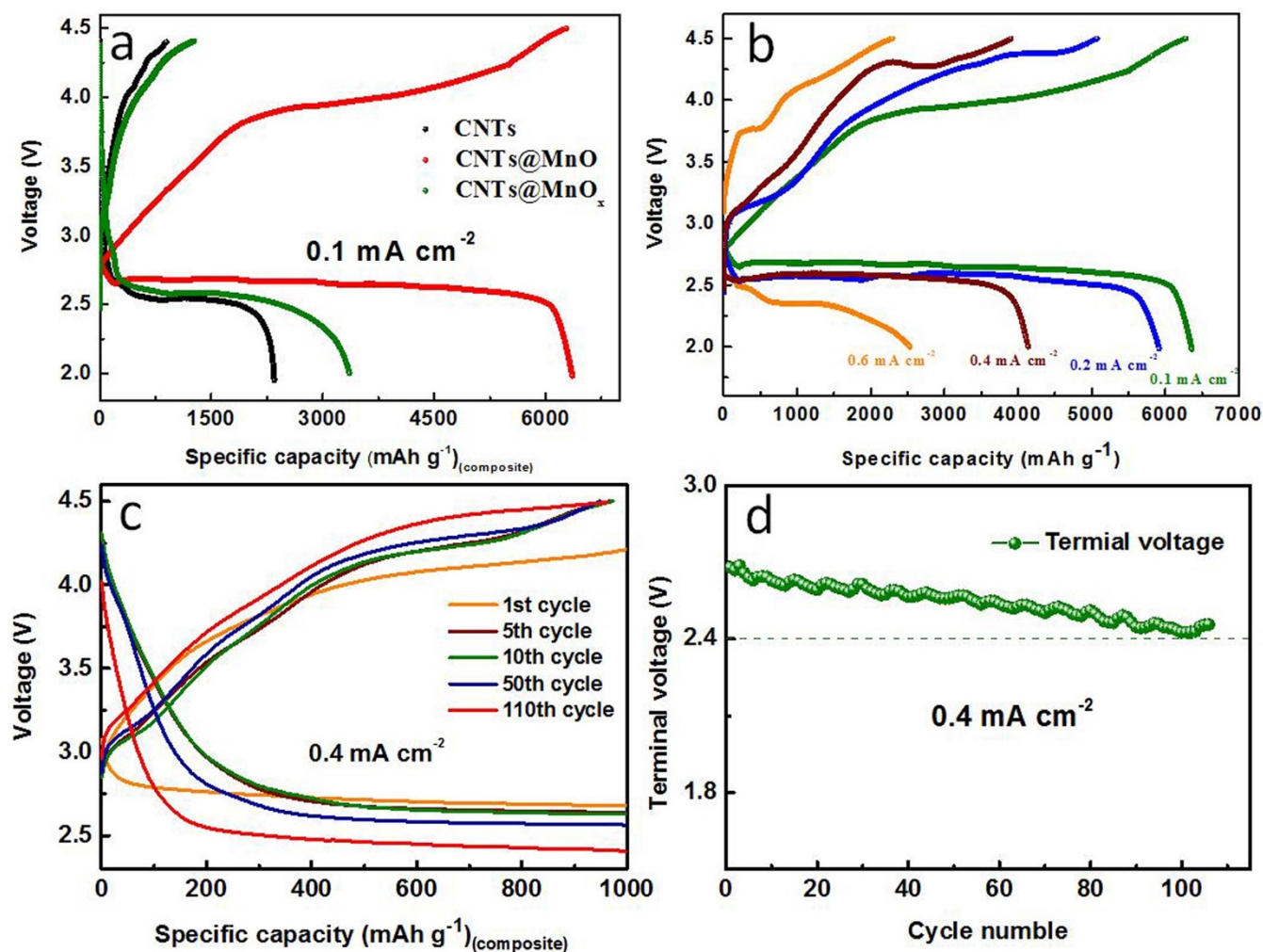

Figure 3 | (a) First discharge-charge curves of the CNTs, and the CNTs@MnO_x and CNTs@MnO composites at 0.1 mA cm^{-2} current density; (b) discharge-charge curves of the CNTs@MnO composite at different current densities; (c) discharge-charge curves for selected cycles of the CNTs@MnO composite at the current density of 0.4 mA cm^{-2} with a fixed capacity of 1000 mAh g^{-1}(composite); (d) variation with cycle number of the discharge terminal voltage at the current density of 0.4 mA cm^{-2} with a fixed capacity of 1000 mAh g^{-1}(composite).
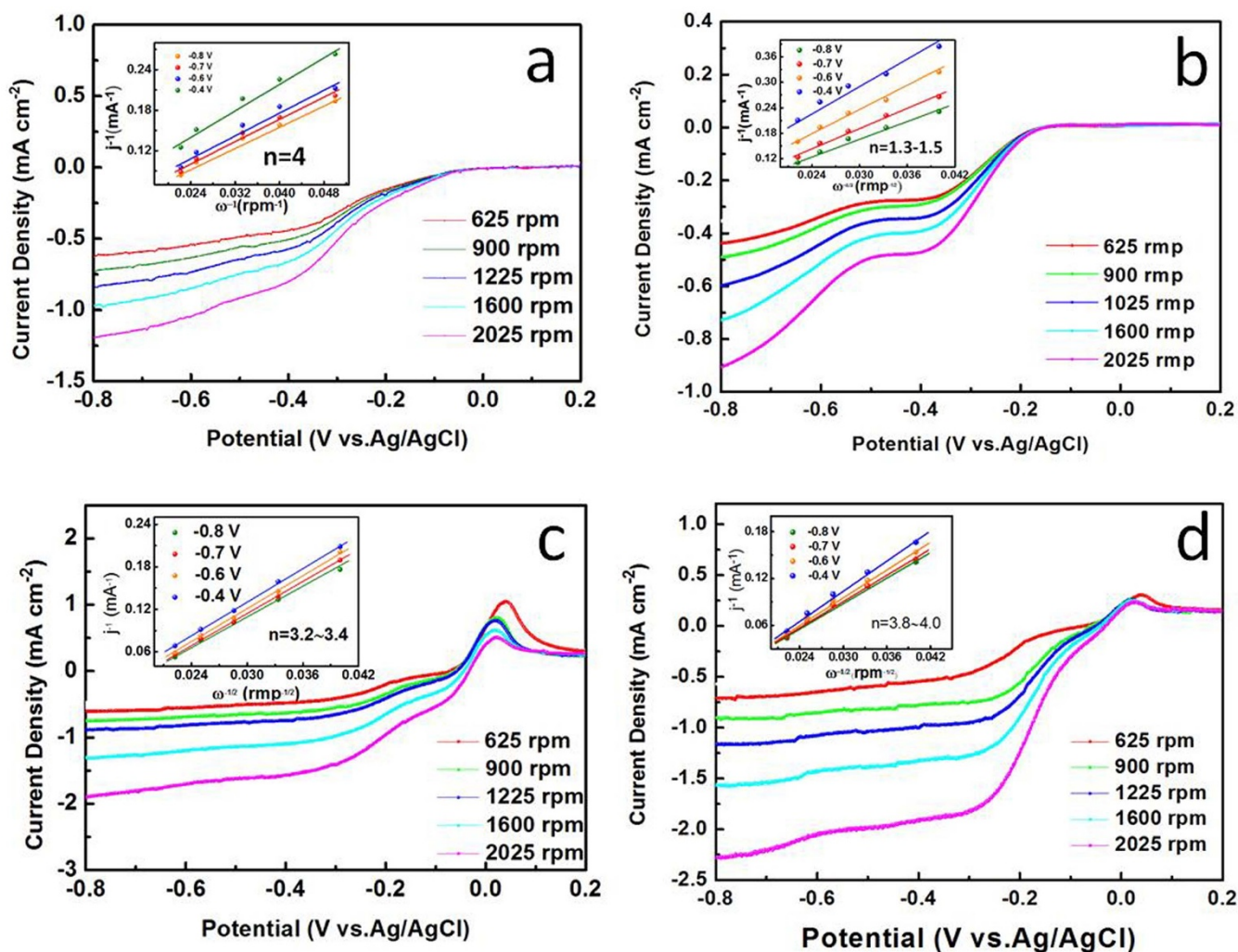
Figure 4 | RDE curves of commercial Pt/C (10 wt% Pt on Vulcan XC-72) (a); CNTs (b); CNTs@MnO$_x$ (c); CNTs@MnO (d) in O$_2$-saturated 0.1 M KOH solution with various rotation speeds and a sweep rate of 5 mV s^{-1}; inset: K–L plots (J^{-1} versus $\omega^{-1/2}$) at different potentials.

2293 mAh g^{-1}(composite) at 0.1, 0.2, 0.4, and 0.6 mA cm^{-2} current densities, respectively, in the fully-discharged stage. Furthermore, the CNTs@MnO composite also shows excellent discharge/charge and cycling performance at 0.4 mA cm^{-2} current density with limited specific capacity of 1000 mAh g^{-1}(composite), with a higher ORR potential as well as a lower OER potential than the other electrodes. The voltage obtained at the discharge terminal is higher than 2.4 V for 100 cycles. Therefore, CNTs@MnO composite is promising for use as a cathode electrocatalyst material for lithium oxygen batteries.

Methods

Synthesis. Preparation of CNTs@MnO composite: commercial multiwalled CNTs (carbon nanotubes, multi-walled, 6–13 nm in outer diameter and 2.5–20 μm in length, Aldrich) were purified by refluxing the as-received sample in 10 wt% nitric acid for 12 h. The acid-treated CNTs were then collected by filtration and dried in vacuum at 120 °C for 12 h. The typical synthesis process for the CNTs@MnO composite can be described as follows. Firstly, 0.2 g CNTs were dispersed in 200 ml deionized (DI) water by ultrasonic vibration for 1 h. 0.32 g KMnO$_4$ was then added into the above suspension, and the mixed solution was stirred by a magnetic bar for 10 h in a round-bottom flask at the temperature of 70 °C. Finally, the product was obtained after centrifugation and washing with water. Then, the obtained black product was dried at 60 °C for 10 h in a vacuum oven, followed by sintering at 500 °C for 6 h under Ar/H$_2$ (95 : 5, v/v) atmosphere to yield the CNTs@MnO.

Characterization. The phase purity and the structural characteristics were analysed by X-ray powder diffraction (GBC MMA) equipped with Cu Kα radiation that was operated over a 2θ range of 5–80° in a continuous scan mode with a scan rate of 2° min^{-1}. The particle size and morphology of the samples were examined using field

emission scanning electron microscopy (FE-SEM; JEOL JSM-7500). Raman spectra were collected using a Raman spectrometer (Jobin Yvon HR800) employing a 10 mW/neon laser at 632.8 nm. The amount of CNTs in the samples was estimated using a Mettler-Toledo thermogravimetric analysis/differential scanning calorimetry (TGA/DSC) STARe System from 50–800 °C at 10 °C min^{-1} in air flux.

Electrochemical measurements. Electrochemical experiments were performed using CR2032 type coin cells with holes in the cathode shell (Fig. S1). For preparing working electrodes, a mixture of the as-synthesized hybrid materials and poly(vinyl difluoride) (PVDF) in a weight ratio of 90 : 10, using 1-methyl-2-pyrrolidinone (NMP) as the solvent, was pasted on the glass microfiber filters which are used for the separator. Typical loadings of cathode powder on 1.1 cm² electrode were ~1.5 mg cm^{-2} (catalyst). The electrolyte consisted of a solution of 1 M LiPF$_6$ in tetraethylene glycol dimethyl ether (TEGDME). Pure lithium foil was used as the counter electrode. The cells were assembled in an argon-filled glove box (Mbraun, Unilab, Germany). Galvanostatic deep-full charge-discharge curves were collected at various current densities of 0.1, 0.2, 0.4, and 0.6 mA cm^{-2} (75, 150, 300, and 450 mA g^{-1}) between 4.5 and 2.0 V vs. Li$^+$/Li, and discharge-charge cycle tests was conducted with 1000 mAh g^{-1} cut off discharge capacity and then charging to 4.4 V vs. Li$^+$/Li. The catalyst stability towards lithium within the voltage window between 2.0–3.5 V was carried out using a lithium ion battery set-up. All tests were conducted on LAND CT 2001A multi-channel battery testers at room temperature in oxygen atmosphere using our specially designed oxygen box. Measurements were repeated at least three times to ensure reliability.

The aqueous rotating disk electrode (RDE) electrochemical tests were carried out using a computer-controlled potentiostat (Princeton 2273 and 616, Princeton Applied Research) with a typical three-electrode cell. A piece of platinum was used as the counter-electrode and an Ag/AgCl (saturated KCl filled) electrode as the reference electrode. The working electrodes were prepared by applying the respective catalyst inks onto the pre-polished glassy carbon (GC) disk electrodes. Briefly, 5 mg sample and 100 μL 5 wt% Nafion® solution were dispersed in 1 mL water/isopropanol (3/1; V/V) solution and ultrasonicated for 30 min to form uniform catalyst inks (~5 mg
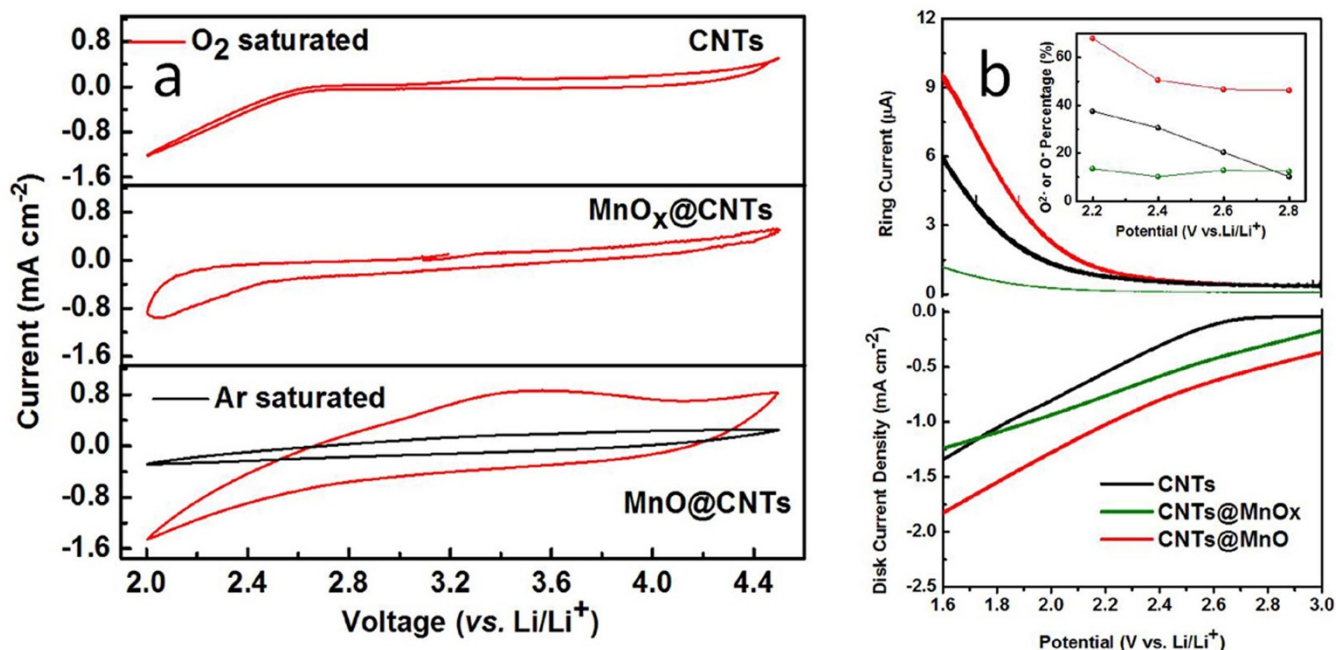
Figure 5 | (a) CV curves acquired at 20 mV s^{-1} in O$_2$ (red line) or Ar (black line) saturated 1 M LiPF$_6$ in TEGDME with 900 rpm rotation speed. (b) RRDE results of the linear sweep voltammograms (LSPs) between 1.6–3.0 V in O$_2$ saturated 1 M LiPF$_6$ in TEGDME acquired at 5 mV s^{-1} with 900 rpm rotation speed.

mL^{-1}). A total of 4.5 μL of well-dispersed catalyst ink was applied onto a pre-polished glassy carbon (GC) disk electrode (5 mm in diameter). The electrodes thus prepared were dried at room temperature overnight prior to the electrochemical tests. The detailed kinetic analysis was conducted according to Koutecky-Levich plots:

$$\frac{1}{j} = \frac{1}{j_k} + \frac{1}{B\omega^{0.5}} \quad (1)$$

where j_k is the kinetic current and B is Levich slope, which is given by:

$$B = 0.2nF(D_{O_2})^{2/3}v^{-1/6}C_{O_2} \quad (2)$$

Here, n is the number of electrons transferred in the reduction of one O$_2$ molecule, F is the Faraday constant ($F = 96485$ C/mol), D_{O_2} is the diffusion coefficient of O$_2$ ($D_{O_2} = 1.9 \times 10^{-5}$ cm^2 s^{-1}), v is the kinematic viscosity for KOH ($v = 0.01$ cm^2 s^{-1}) and

C_{O_2} is concentration of O$_2$ in the solution ($C_{O_2} = 1.2 \times 10^{-6}$ mol cm^{-3}). The constant 0.2 is adopted when the rotation speed is expressed in rpm. According to Equations (1) and (2), the number of electrons transferred (n) can be obtained from the slope of Koutecky-Levich plot of i^{-1} vs. $\omega^{-1/2}$.

The non-aqueous rotating ring-disk electrode (RRDE) electrochemical tests and the cyclic voltammetry (CV) were carried out using computer-controlled potentiostats (Princeton 2273 and 636, Princeton Applied Research, Arbin BT2000). A lithium foil embedded inside nickel foam was used as the counter-electrode and reference electrode. The working electrodes were prepared using the same procedure as described above. A total of 5.5 μL of well-dispersed catalyst ink was applied onto a pre-polished glassy carbon (GC) disk electrode (5.61 mm in diameter). The electrodes thus prepared were dried at room temperature overnight prior to the electrochemical tests. Cyclic voltammograms (CV) in non-aqueous electrolyte were obtained between 2 V and 4.5 V at various rotation speeds from 400 to 2700 rpm in
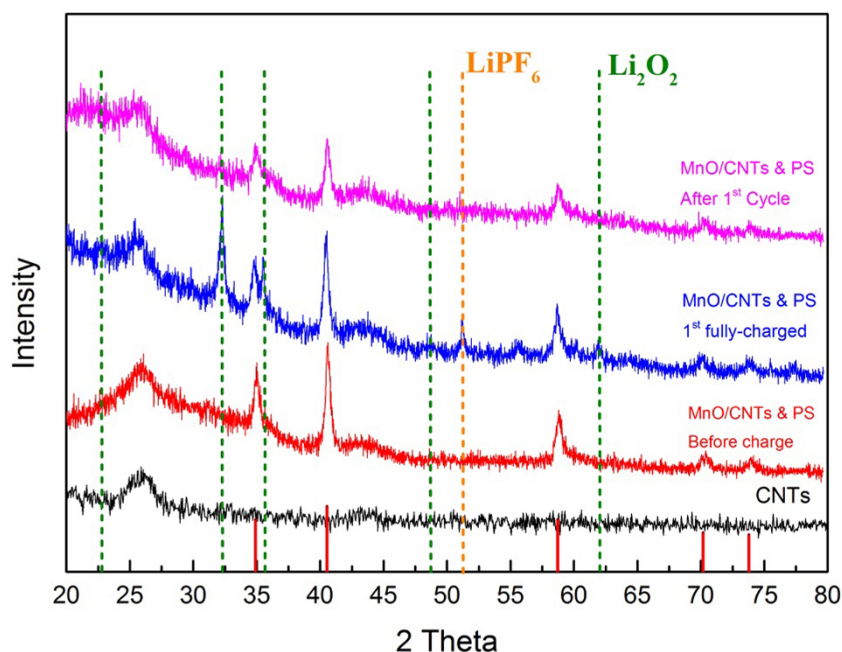

Figure 6 | XRD patterns for different charge and discharge states of the CNTs@MnO composite coating on the glass fiber separator (GFS).
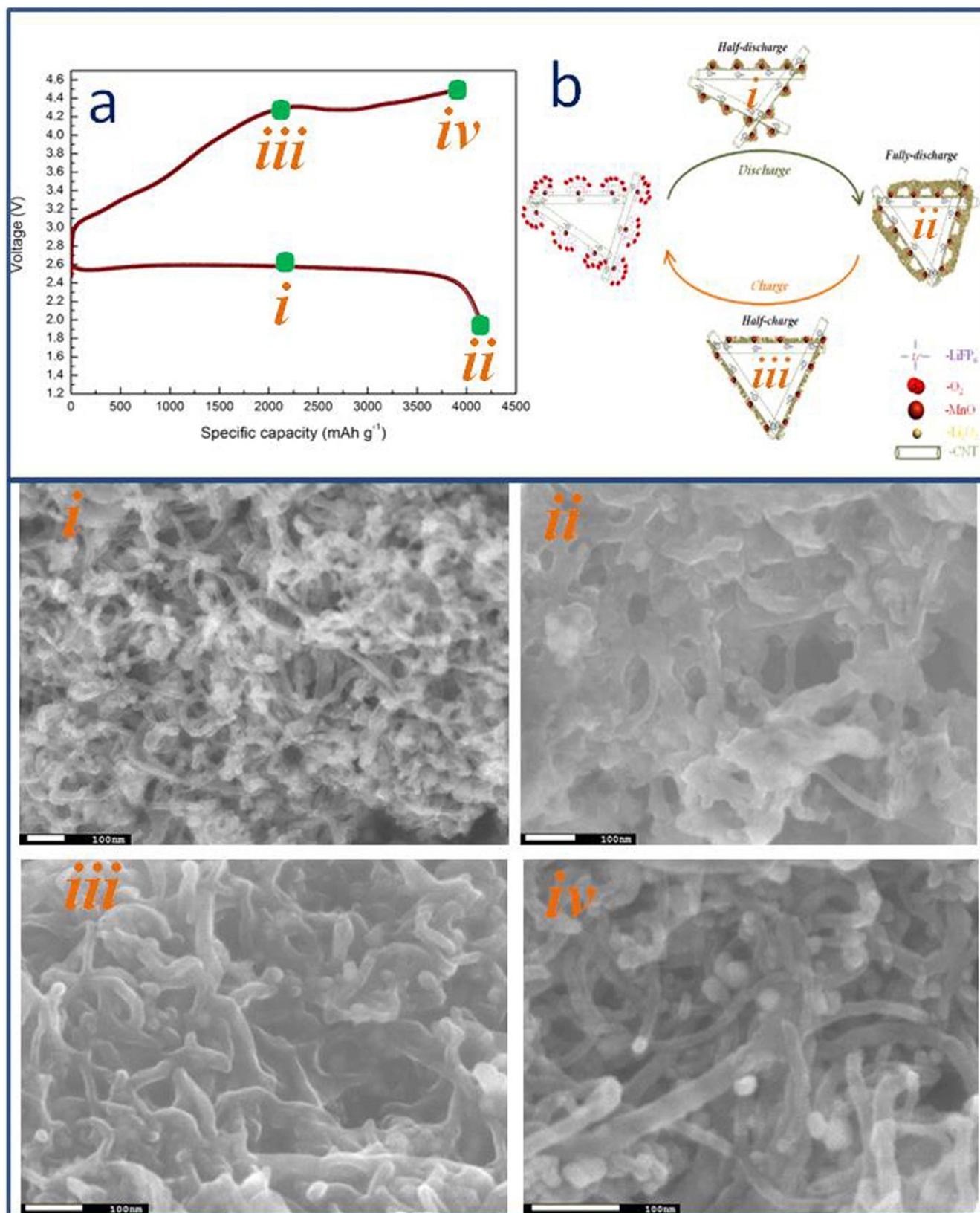
Figure 7 | SEM images at different charge and discharge states of the CNTs@MnO composite at the current density of 0.4 mA cm^{-2} (i–iv); and a schematic diagram of the whole process of discharge and charge (b).

O$_2$ saturated electrolyte. Working electrodes were first prepared by the procedure described above in the electrode preparation section. The working electrode was immersed in Ar-purged electrolyte for 20 minutes prior to each cyclic voltammetry experiment. After steady-state CVs were obtained in Ar (2.0–4.5 V, 20 mV s^{-1}), the cell was purged with O$_2$ for 20 min, and similar CVs were obtained in O$_2$-saturated electrolyte at 20 mV s^{-1} at various rotation speeds. Linear sweep voltammograms (LSPs) were collected between 1.6 – 3.0 V with a scan rate of 5 mV s^{-1} at 900 rpm in O$_2$-saturated electrolyte, with the ring held at 3.5 V.

1. Christensen, J. *et al.* A Critical Review of Li/Air Batteries. *J Electrochem Soc* **159**, R1–R30, doi:Doi 10.1149/2.086202jes (2012).
2. Hassoun, J. *et al.* A Metal-Free, Lithium-Ion Oxygen Battery: A Step Forward to Safety in Lithium-Air Batteries. *Nano Lett* **12**, 5775–5779, doi:Doi 10.1021/Nl303087j (2012).
3. Park, M., Sun, H., Lee, H., Lee, J. & Cho, J. Lithium-Air Batteries: Survey on the Current Status and Perspectives Towards Automotive Applications from a Battery Industry Standpoint. *Adv Energy Mater* **2**, 780–800, doi:DOI 10.1002/aenm.201200020 (2012).
4. Wang, Y. G. & Xia, Y. Y. Li-O₂ Batteries an Agent for Change. *Nat Chem* **5**, 445–447 (2013).
5. Bruce, P. G., Freunberger, S. A., Hardwick, L. J. & Tarascon, J. M. Li-O₂ and Li-S batteries with high energy storage. *Nat Mater* **11**, 19–29, doi:Doi 10.1038/Nmat3191 (2012).
6. Zhang, T. & Zhou, H. S. A reversible long-life lithium-air battery in ambient air. *Nat Commun* **4**, 1817(1–7), DOI: 10.1038/ncomms2855 (2013).
7. Black, R., Adams, B. & Nazar, L. F. Non-Aqueous and Hybrid Li-O₂ Batteries. *Adv Energy Mater* **2**, 801–815, doi:DOI 10.1002/aenm.201200001 (2012).
8. Eom, H. R., Kim, M. K., Kim, M. S., Kim, G. P. & Baeck, S. H. Synthesis and Characterizations of MnO₂/Multi-Wall Carbon Nanotubes Nanocomposites for Lithium-Air Battery. *J Nanosci Nanotechnol* **13**, 1780–1783 (2013).
9. Lim, H. D. *et al.* Mechanism of Co₃O₄/graphene catalytic activity in Li-O₂ batteries using carbonate based electrolytes. *Electrochim Acta* **90**, 63–70, doi:DOI 10.1016/j.electacta.2012.12.020 (2013).
10. Cheng, H. & Scott, K. Carbon-supported manganese oxide nanocatalysts for rechargeable lithium-air batteries. *J Power Sources* **195**, 1370–1374, doi:DOI 10.1016/j.jpowsour.2009.09.030 (2010).
11. Li, Y. L. *et al.* Nitrogen-doped carbon nanotubes as cathode for lithium-air batteries. *Electrochem Commun* **13**, 668–672, doi:DOI 10.1016/j.elecom.2011.04.004 (2011).
12. Xiao, J. *et al.* Hierarchically Porous Graphene as a Lithium-Air Battery Electrode. *Nano Lett* **11**, 5071–5078, doi:Doi 10.1021/Nl203332e (2011).
13. Mitchell, R. R., Gallant, B. M., Thompson, C. V. & Shao-Horn, Y. All-carbon-nanofiber electrodes for high-energy rechargeable Li-O₂ batteries. *Energ Environ Sci* **4**, 2952–2958 (2011).
14. Wu, G. *et al.* Nitrogen Doped Graphene-Rich Catalysts Derived from Heteroatom Polymers for Oxygen Reduction in Nonaqueous Lithium-O₂ Battery Cathodes. *Acs Nano* **6**, 9764–9776, doi:Doi 10.1021/Nn303275d (2012).
15. Atienza, D. O., Allison, T. C. & Tong, Y. Y. J. Spatially Resolved Electronic Alterations As Seen by in Situ Pt-195 and (CO)-C-13 NMR in Ru@Pt and Au@Pt Core-Shell Nanoparticles. *J Phys Chem C* **116**, 26480–26486, doi:Doi 10.1021/Jp310313k (2012).
16. Thapa, A. K. *et al.* Gold-Palladium nanoparticles supported by mesoporous beta-MnO₂ air electrode for rechargeable Li-Air battery. *J Power Sources* **220**, 211–216 (2012).
17. Lu, Y. C. *et al.* Platinum-Gold Nanoparticles: A Highly Active Bifunctional Electrocatalyst for Rechargeable Lithium-Air Batteries. *J Am Chem Soc* **132**, 12170–12171 (2010).
18. Peng, Z. Q., Freunberger, S. A., Chen, Y. H. & Bruce, P. G. A Reversible and Higher-Rate Li-O₂ Battery. *Science* **337**, 563–566, doi:DOI 10.1126/science.1223985 (2012).
19. Jung, H. G. *et al.* Ruthenium-Based Electrocatalysts Supported on Reduced Graphene Oxide for Lithium-Air Batteries. *ACS Nano* **7**, 3532–3539, doi:Doi 10.1021/Nn400477d (2013).
20. Debart, A., Paterson, A. J., Bao, J. & Bruce, P. G. alpha-MnO₂ nanowires: A catalyst for the O₂ electrode in rechargeable lithium batteries. *Angew Chem, Int Ed* **47**, 4521–4524, doi:DOI 10.1002/anie.200705648 (2008).
21. Zhang, L. X. *et al.* Mesoporous NiCo₂O₄ nanoflakes as electrocatalysts for rechargeable Li-O₂ batteries. *Chem Commun* **49**, 3540–3542, doi:Doi 10.1039/C3cc40393a (2013).
22. Li, J. X., Wang, N., Zhao, Y., Ding, Y. H. & Guan, L. H. MnO₂ nanoflakes coated on multi-walled carbon nanotubes for rechargeable lithium-air batteries. *Electrochem Commun* **13**, 698–700, doi:DOI 10.1016/j.elecom.2011.04.013 (2011).
23. Lim, S. H., Kim, B. K. & Yoon, W. Y. Catalytic behavior of V₂O₅ in rechargeable Li-O₂ batteries. *J Appl Electrochem* **42**, 1045–1048, doi:DOI 10.1007/s10800-012-0480-7 (2012).
24. Yang, W. *et al.* Perovskite Sr₀.₉₅Ce₀.₀₅CoO₃₋δ loaded with copper nanoparticles as a bifunctional catalyst for lithium-air batteries. *J Mater Chem* **22**, 18902–18907, doi:Doi 10.1039/C2jm33440b (2012).
25. Ling, C. & Mizuno, F. Capture Lithium in alpha-MnO₂: Insights from First Principles. *Chem Mater* **24**, 3943–3951, doi:Doi 10.1021/Cm302347j (2012).
26. Chen, Y., Freunberger, S. A., Peng, Z., Barde, F. & Bruce, P. G. Li-O₂ Battery with a Dimethylformamide Electrolyte. *J Am Chem Soc* **134**, 7952–7957, doi:Doi 10.1021/Ja302178w (2012).
27. Jung, H. G., Hassoun, J., Park, J. B., Sun, Y. K. & Scrosati, B. An improved high-performance lithium-air battery. *Nat Chem* **4**, 579–585, doi:Doi 10.1038/Nchem.1376 (2012).
28. Shui, J. L., Karan, N. K., Balasubramanian, M., Li, S. Y. & Liu, D. J. Fe/N/C Composite in Li-O₂ Battery: Studies of Catalytic Structure and Activity toward Oxygen Evolution Reaction. *J Am Chem Soc* **134**, 16654–16661, doi:Doi 10.1021/Ja3042993 (2012).
29. Liu, C., Li, F., Ma, L. P. & Cheng, H. M. Advanced Materials for Energy Storage. *Adv Mater* **22**, E28–+, doi:DOI 10.1002/adma.200903328 (2010).
30. Wu, Z. S. *et al.* 3D Nitrogen-Doped Graphene Aerogel-Supported Fe₃O₄ Nanoparticles as Efficient Eletrocatalysts for the Oxygen Reduction Reaction. *J Am Chem Soc* **134**, 9082–9085, doi:Doi 10.1021/Ja3030565 (2012).
31. Liang, Y. Y. *et al.* Covalent Hybrid of Spinel Manganese-Cobalt Oxide and Graphene as Advanced Oxygen Reduction Electrocatalysts. *J Am Chem Soc* **134**, 3517–3523 (2012).
32. Liang, Y. Y. *et al.* Co₃O₄ nanocrystals on graphene as a synergistic catalyst for oxygen reduction reaction. *Nat Mater* **10**, 780–786 (2011).
33. Mayrhofer, K. J. J. *et al.* Measurement of oxygen reduction activities via the rotating disc electrode method: From Pt model surfaces to carbon-supported high surface area catalysts. *Electrochim Acta* **53**, 3181–3188, doi:DOI 10.1016/j.electacta.2007.11.057 (2008).
34. Lu, Y. C., Gasteiger, H. A., Crumlin, E., McGuire, R. & Shao-Horn, Y. Electrocatalytic Activity Studies of Select Metal Surfaces and Implications in Li-Air Batteries. *J Electrochem Soc* **157**, A1016–A1025, doi:Doi 10.1149/1.3462981 (2010).
35. McGuire, R., Jr. *et al.* Oxygen reduction reactivity of cobalt(ii) hangman porphyrins. *Chem Sci* **1**, 411–414, doi:10.1039/c0sc00281j (2010).
36. Calvo, E. J. & Mozhzhukhina, N. A rotating ring disk electrode study of the oxygen reduction reaction in lithium containing non aqueous electrolyte. *Electrochem Commun* **31**, 56–58, doi:DOI 10.1016/j.elecom.2013.03.005 (2013).
37. Laoire, C. O., Mukerjee, S., Abraham, K. M., Plichta, E. J. & Hendrickson, M. A. Elucidating the Mechanism of Oxygen Reduction for Lithium-Air Battery Applications. *J Phys Chem C* **113**, 20127–20134 (2009).
38. Hou, J. B., Yang, M., Ellis, M. W., Moore, R. B. & Yi, B. L. Lithium oxide precipitation in nonaqueous Li-air batteries. *Phys Chem Chem Phys* **14**, 13487–13501, doi:Doi 10.1039/C2cp42768k (2012).
39. Wang, Y. R. *et al.* Nano- and micro-sized TiN as the electrocatalysts for ORR in Li-air fuel cell with alkaline aqueous electrolyte. *J Mater Chem* **22**, 15549–15555, doi:Doi 10.1039/C2jm32681g (2012).

Acknowledgments

Author contributions

W.L. and S.C. designed the experiments and discussed the interpretation of results. W.L., S.C., J.W., Y.Z. and H.L. discussed the results, and participated in the manuscript revision. All authors reviewed the manuscript.

Additional information